# Supplemental Material

## Fundamental precision bounds for three-dimensional optical localization microscopy with Poisson statistics

Mikael P. Backlund, Yoav Shechtman, Ronald L. Walsworth

# I. ADDITIONAL FIGURES

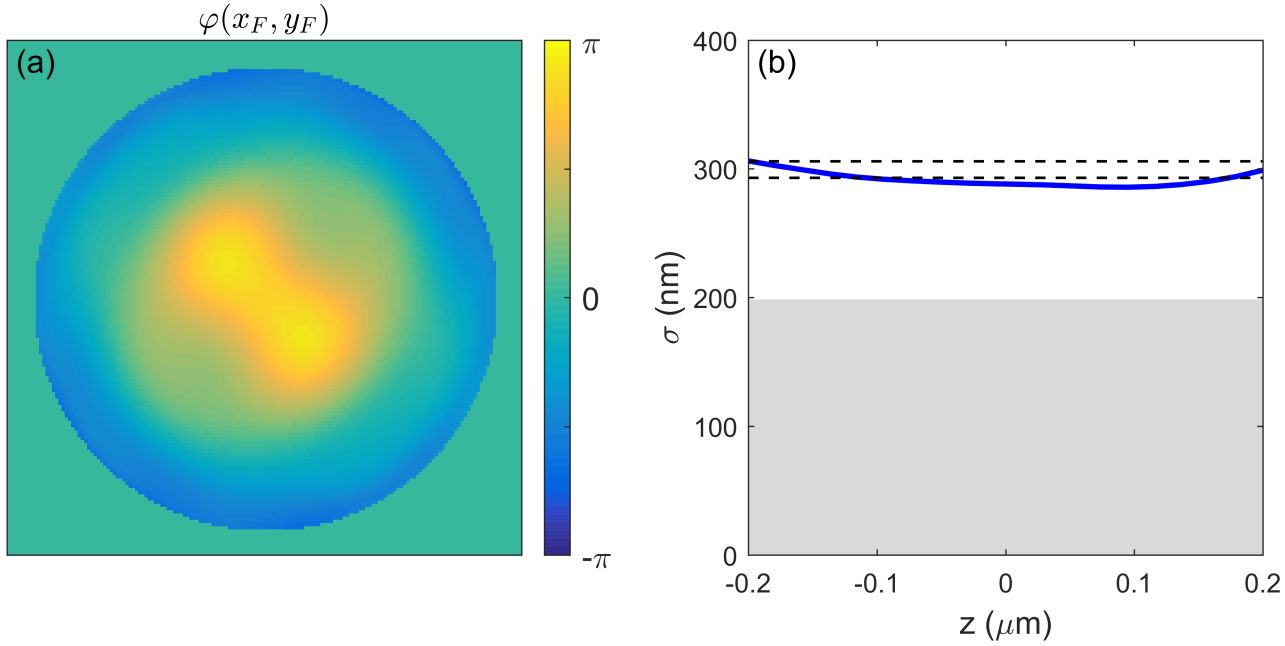



FIG. S1. Results of PSF optimization by minimization of $\sigma_z^{(\mathrm{CRB})}$. We employed the same basic algorithm as was used previously to produce the Saddle-Point [1] and Tetrapod [2] family of PSFs. Key differences here are that we assume zero background light and we proceed via minimization of the average value of $\sigma_z^{(\mathrm{CRB})}$ over a specified range in $z$, rather than minimizing $\sqrt{\left(\sigma_x^{(\mathrm{CRB})}\right)^2 + \left(\sigma_y^{(\mathrm{CRB})}\right)^2 + \left(\sigma_z^{(\mathrm{CRB})}\right)^2}$. We choose a relatively narrow range in $z$ of 400 nm in order to push toward optimal local CRB, as there is known to be a tradeoff between $z$ range and precision [2]. For consistency here we assume NA = 1.4, $\lambda_\circ$ = 670 nm, and matched immersion index of $n = 1.518$. (a) Phase mask $\varphi(x_F, y_F)$ resulting from optimization. (b) $\sigma_z^{(\mathrm{CRB})}$ of optimized PSF (blue line). Gray box is bounded above by $\sigma_z^{(\mathrm{QCRB})}$. Lower dashed black line is the minimum $\sigma_z^{(\mathrm{CRB})}$ of the standard PSF, while upper dashed black line is the minimum $\sigma_z^{(\mathrm{CRB})}$ of an astigmatic PSF with strength $A_{\mathrm{astig.}} = 1$ (see Fig. S2).

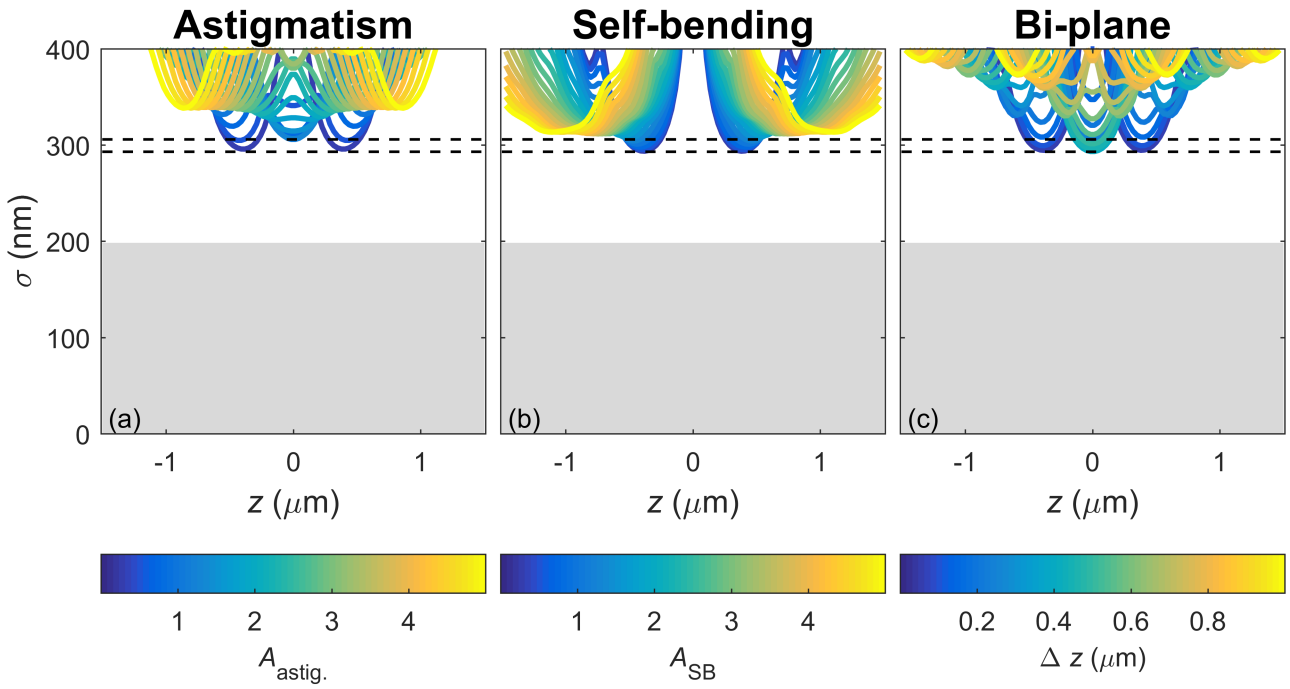



FIG. S2. Comparison of single-objective $\sigma_z^{(\mathrm{QCRB})}$ (gray boxes) to $\sigma_z^{(\mathrm{CRB})}$ obtained by several types of engineered microscopes. In each panel the lower dashed black line is the minimum $\sigma_z^{(\mathrm{CRB})}$ obtained by the standard PSF, while the upper dashed black line is the minimum $\sigma_z^{(\mathrm{CRB})}$ obtained by astigmatic imaging with strength described in the main text. (a) Various strengths of astigmatic imaging [3]. We assume the wavefunction $\psi(x_F, y_F)$ is multiplied by a phase factor $\exp[i\varphi(x_F, y_F)]$ before being focused by a lens to a camera placed at the image plane. Here $\varphi(x_F, y_F) = A_{\mathrm{astig.}}\sqrt{6}(x_F^2 - y_F^2)$ with the strength $A_{\mathrm{astig.}}$ varied as indicated by the colorbar. (b) Imaging with various strengths of the self-bending PSF [4]. Again we assume the wavefunction $\psi(x_F, y_F)$ is multiplied by a phase factor $\exp[i\varphi(x_F, y_F)]$ before being focused by a lens to a camera placed at the image plane, but now with $\varphi(x_F, y_F) = A_{\mathrm{SB}}[(x_F + y_F)^3 + (x_F - y_F)^3]$ and $A_{\mathrm{SB}}$ indicated by the colorbar. (c) Bi-plane imaging [5]. The wavefunction is split by a 50/50 beam splitter, then an equal and opposite amount of defocus is introduced into each of the two output channels before focusing with two lenses onto two cameras placed at the image planes. Mathematically: $\psi(x_F, y_F) \to \psi\left(x_F^+, y_F^+\right) \exp\left[ik\Delta z\sqrt{1 - \left(r_F^+\right)^2}\right]/\sqrt{2} + i\psi\left(-x_F^-, y_F^-\right) \exp\left[-ik\Delta z\sqrt{1 - \left(r_F^-\right)^2}\right]/\sqrt{2}$. The parameter $\Delta z$ is varied as indicated by the colorbar.

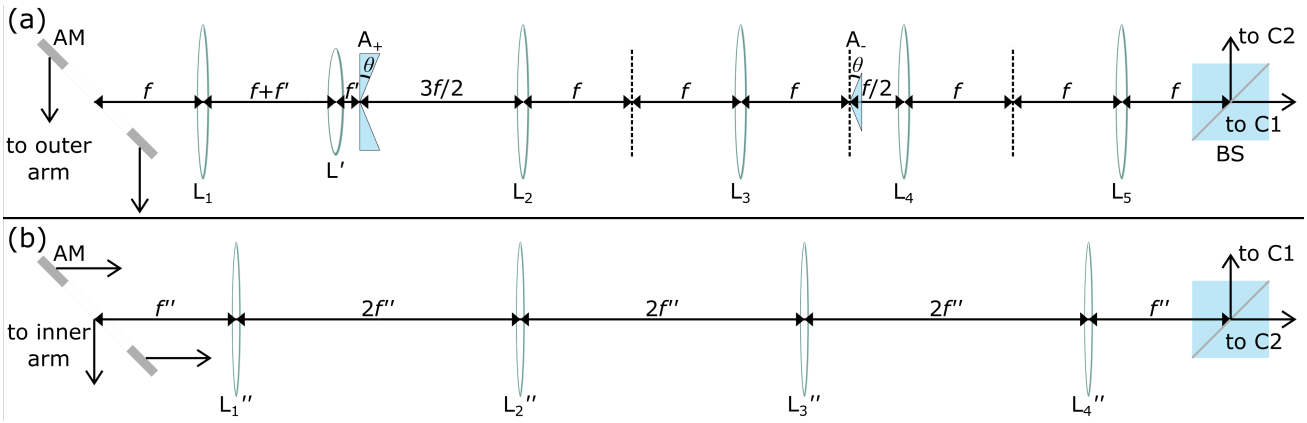



FIG. S3. Schematic of radial shear interferometer showing unfolded arms of the interferometer and exact distances between optical elements. (a) Unfolded inner arm including annular mirror (AM), lenses $\mathrm{L}_i$ with focal length $f = 200$ mm, lens $\mathrm{L}'$ with focal length $f' = 44$ mm, positive-phase axicon ($\mathrm{A}_+$), negative-phase axicon ($\mathrm{A}_-$), and beam splitter (BS). (b) Unfolded outer arm including lenses $\mathrm{L}''_j$ with focal length $f = 261$ mm.

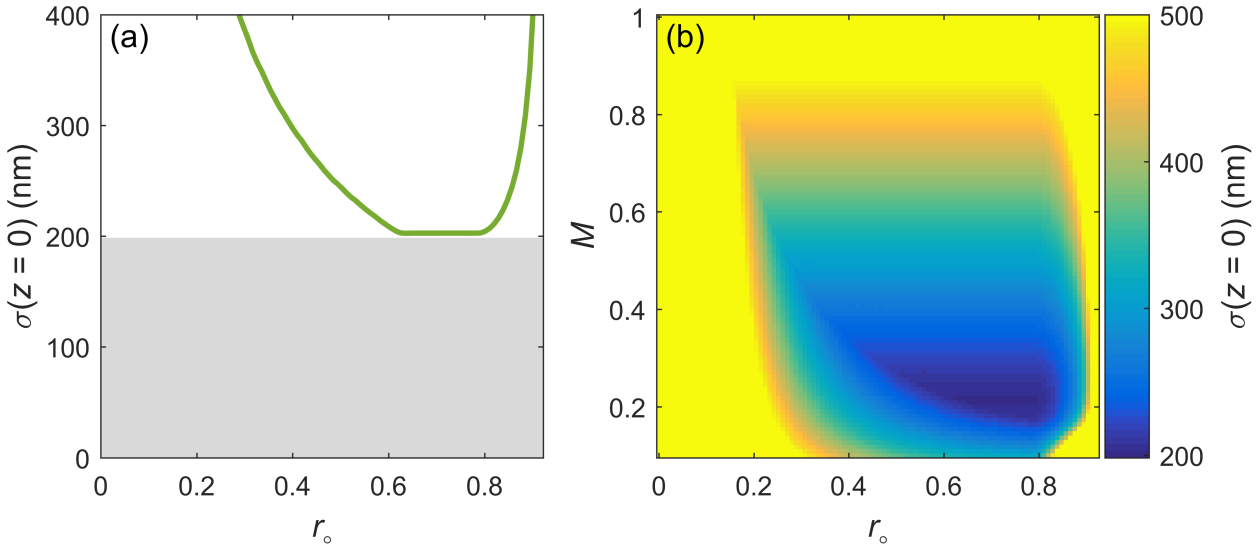



FIG. S4. $\sigma_z^{(\mathrm{CRB})}$ evaluated at $z = 0$ for radial shear interferometer as a function of the parameters $r_\circ$ and $M$. (a) One-dimensional slice of the function for fixed $M$ and variable $r_\circ$ (green line). Gray box again indicates region below $\sigma_z^{(\mathrm{QCRB})}$. (b) Two-dimensional depiction of the function. Minimum of the colormap corresponds to $\sigma_z^{(\mathrm{QCRB})}$. The maximum value of the colormap is set to match the dynamic range of the interesting region, at the expense of saturating the outer portion.

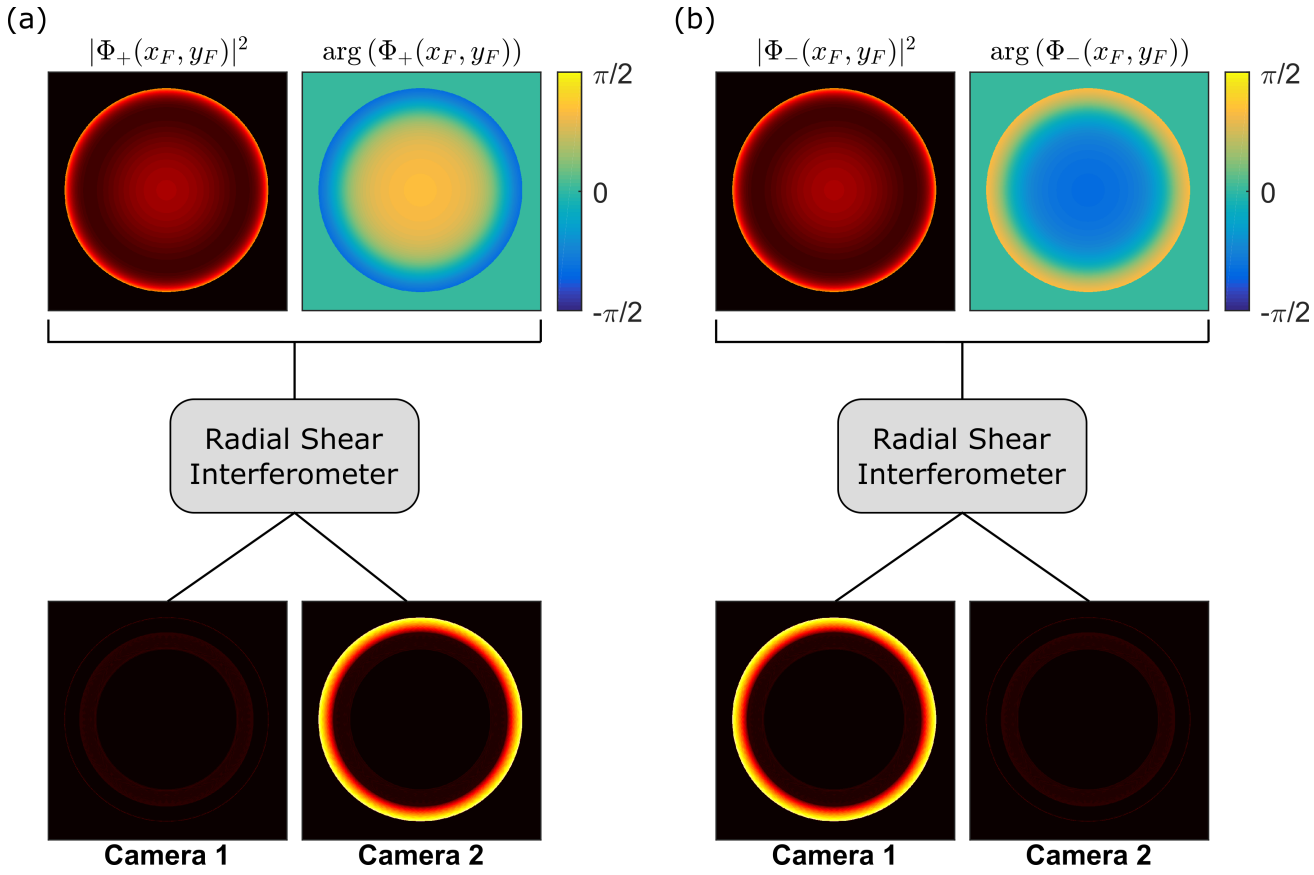



FIG. S5. Schematic depicting how the radial shear interferometer relates to projections onto the eigenstates of $\mathcal{L}_z$ for the single objective case. These eigenstates $|\Phi_+\rangle$ and $|\Phi_-\rangle$ and their associated classical wavefunctions $\Phi_+(x_F, y_F)$ and $\Phi_-(x_F, y_F)$ are described in Section III. (a) Top: intensity and phase associated with $\Phi_+$. Inputting $\Phi_+$ to the radial shear interferometer results in an output (bottom) in which most of the light is incident on Camera 2 and relatively little on Camera 1. Thus the interferometer approximates a projection onto the state $|\Phi_+\rangle$. (b) Top: intensity and phase associated with $\Phi_-$. Note the same intensity and opposite phase as in (a). Inputting $\Phi_-$ to the radial shear interferometer results in an output (bottom) in which most of the light is incident on Camera 1 and relatively little on Camera 2. Thus the interferometer approximates an orthogonal projection onto the state $|\Phi_-\rangle$.

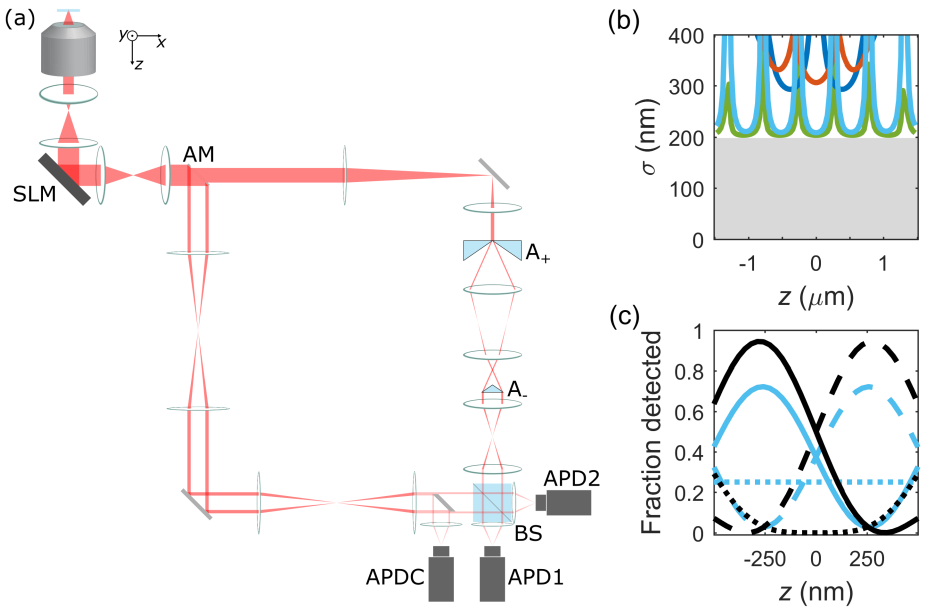



FIG. S6. A variation of the radial shear interferometer in which three point detectors, e.g., avalanche photodiodes (APD), are used instead of two cameras. (a) Schematic of setup showing the output ports of the beam splitter focused onto detectors APD1 and APD2. A mirror of radius $(\mathrm{NA}/n - Mr_\circ)$ is added to the outer arm just before the beam splitter in order to pick off the light that has no counterpart in the inner arm. This light is detected on a complementary detector APDC. (b) Photon-normalized precision bounds of $z$ estimation for single-objective case. Gray box indicates region below $\sigma_z^{(\mathrm{QCRB})}$. Lines indicate standard PSF (blue), astigmatism of the same strength described in the main text (red), the two-camera radial shear interferometer (green), and the three-APD radial shear interferometer depicted in (a) (cyan). The minimum of the three-APD variant is approximately $1.05 \times \sigma_z^{(\mathrm{QCRB})}$, slightly worse than the minimum of the two-camera version of approximately $1.03 \times \sigma_z^{(\mathrm{QCRB})}$. (c) Comparison of the three detection channels of the three-APD radial shear interferometer (cyan) and the optimal measurement of projection onto the eigenstates of $\mathcal{L}_z$ (black; see Section III). For cyan lines, solid is the expected fraction of photons detected on APD1, dashed is that for APD2, and dotted is that for APDC. For black lines, solid indicates $|\langle\Phi_-|\psi\rangle|^2$, dashed is $|\langle\Phi_+|\psi\rangle|^2$, and dotted is $1 - |\langle\Phi_-|\psi\rangle|^2 - |\langle\Phi_+|\psi\rangle|^2$. Here $|\Phi_+\rangle$ and $|\Phi_-\rangle$ are chosen to resolve $\mathcal{L}_z$ in a region near $z = 0$, as explained in Section III.

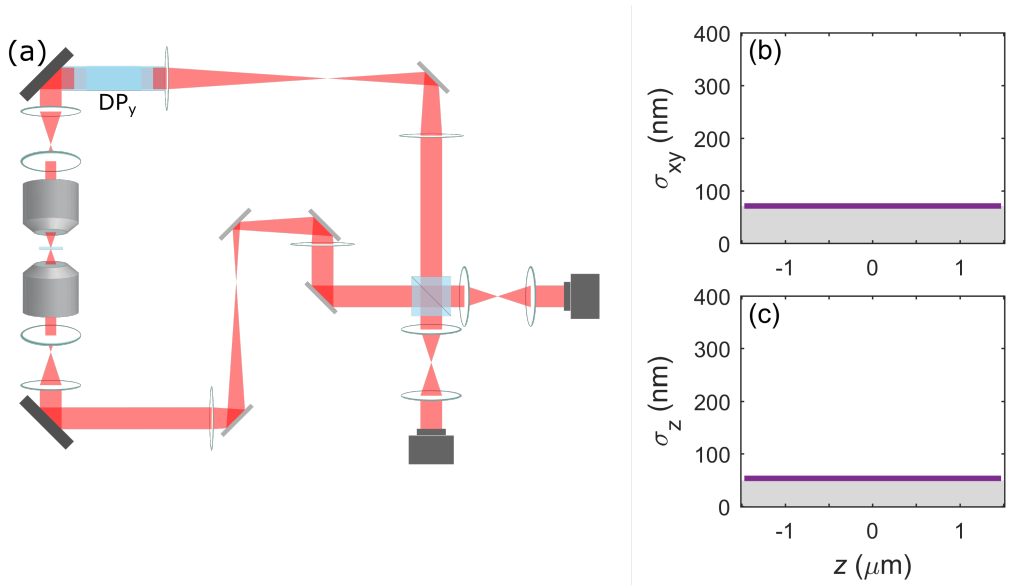



FIG. S7. Variant of dual-objective interferometric measurement analyzed in Section VI. (a) Schematic of apparatus. Compared to the scheme described in the main text, this variant places the detectors at conjugate Fourier planes rather than image planes. Thus an additional lens is placed in each output channel. The Dove prism ($DP_y$) is rotated 90 degrees to produce an additional reflection in $y$ in order to maintain optimality of the measurement in this configuration (linear phases must now be opposed to produce an interference pattern in the Fourier plane). (b) Photon-normalized $x, y$ localization precision (purple). It saturates $\sigma_{x,y}^{(\mathrm{QCRB})}$(gray box). (c) Photon-normalized $z$ localization precision (purple). It saturates $\sigma_z^{(\mathrm{QCRB})}$ (gray box).

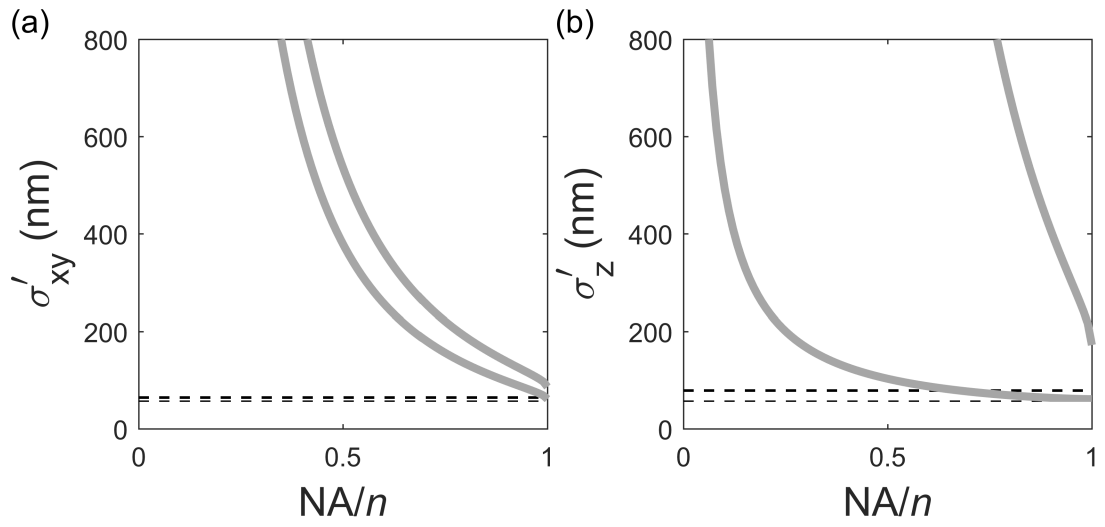



FIG. S8. Comparison of bounds derived in this work to those given by Eqs. (21-24) in Ref. [6], for both lateral precision (a) and axial precision (b). In both plots the the black dashed lines are the constant (i.e. they do not depend on NA) bounds presented in Ref. [6]. There are two such bounds presented: one for a $z$-oriented linearly polarized dipole and one for a circularly polarized dipole in the $xy$ plane. The bounds presented in the current work are depicted by the solid gray lines. In both panels the lower gray line corresponds to the dual-objective $\sigma^{(\mathrm{QCRB})}$ and the higher line corresponds to the single-objective $\sigma^{(\mathrm{QCRB})}$. Now, in Ref. [6] the bounds are given as functions of the number of photons emitted by the source, rather than the number of photons collected. Thus for accurate comparison, our expressions must be multiplied by a geometrical factor $\chi_1 = \sqrt{4\pi\mathcal{A}^2}$ for single-objective collection and $\chi_2 = \sqrt{2\pi\mathcal{A}^2}$ for dual-objective collection. The plots above then show $\sigma' = \sigma^{(\mathrm{QCRB})} \times \chi_{1,2}$ as a function of NA/$n$. Since the dashed black lines assume no constraints imposed by collection geometry, their minima should bound the gray solid lines. Indeed this is the case. That the minima of the gray solid lines lie between the two dashed lines is consistent with the fact that unpolarized, isotropic emission (considered in our work) can be represented as a statistical mixture of radiation due to dipoles of orthogonal polarizations [7]. These plots show that the expressions presented in our work will give tighter bounds when comparing to experimental measurements using one or two microscope objectives. Furthermore, the difference between our expressions and the bounds of Ref. [6] are more than just a trivial collection factor $\chi_{1,2}$ that scales with NA, as evinced most clearly by the nontrivial relation between the solid gray lines in panel (b).

## II. DERIVATION OF SINGLE-OBJECTIVE QCRB

Here we derive the QFI and QCRB for localization with single-objective collection. We consider the one-photon state given by $\rho = |\psi\rangle\langle\psi|$, with $|\psi\rangle$ defined by:

$$|\psi\rangle = \iint \mathrm{d}A_F \psi\left(x_F, y_F; \mathbf{x}\right)|x_F, y_F\rangle \,, \tag{S1}$$

and

$$\psi\left(x_F, y_F; \mathbf{x}\right) = \mathcal{A}\left(1 - r_F^2\right)^{-1/4} \mathrm{Circ}\left(\frac{n r_F}{NA}\right) \exp\left[ik\left(x x_F + y y_F + z\sqrt{1 - r_F^2}\right)\right]. \tag{S2}$$

Since $\rho = |\psi\rangle\langle\psi|$ describes a pure state, we could save some algebra and compute the QFI directly from:

$$\mathcal{K}_{ij} = 4\left[\mathrm{Re}\,\langle\partial_i\psi|\partial_j\psi\rangle + \langle\partial_i\psi|\psi\rangle\langle\partial_j\psi|\psi\rangle\right], \tag{S3}$$

which is proportional to the Fubini-Study metric [8]. We instead choose to first find expressions for the symmetric logarithmic derivative operators (SLDs) and proceed as described in the main text, as the SLDs will be referenced in the next Section. The SLDs are given implicitly by the relations:

$$\partial_x \rho = \frac{1}{2}\left(\mathcal{L}_x \rho + \rho \mathcal{L}_x\right), \tag{S4a}$$

$$\partial_y \rho = \frac{1}{2}\left(\mathcal{L}_y \rho + \rho \mathcal{L}_y\right), \tag{S4b}$$

$$\partial_z \rho = \frac{1}{2}\left(\mathcal{L}_z \rho + \rho \mathcal{L}_z\right), \tag{S4c}$$

where $\partial_{x_i}\rho = |\partial_{x_i}\psi\rangle\langle\psi| + |\psi\rangle\langle\partial_{x_i}\psi|$ for each $i$.

Let $\{|l\rangle\}$ be the set of eigenstates of $\rho$ with corresponding eigenvalues $\{D_l\}$. In this basis each $\mathcal{L}_{x_i} \in \{\mathcal{L}_x, \mathcal{L}_y, \mathcal{L}_z\}$ can be defined explicitly [9]:

$$\mathcal{L}_{x_i} = \sum_{l,l';D_l + D_{l'} \neq 0} \frac{2}{D_l + D_{l'}} \langle l|\partial_{x_i}\rho|l'\rangle\, |l\rangle\langle l'| \,. \tag{S5}$$

Clearly $|\psi\rangle$ is one eigenstate of $\rho$ with eigenvalue 1. All other eigenstates of $\rho$ have eigenvalue 0. States $|l\rangle$ for which $\rho|l\rangle = \mathbf{0}$ contribute to the sum in Eq. (S5) if $(\partial_{x_i}\rho)|l\rangle \neq \mathbf{0}$

for some $i$. Consider the state vectors:

$$|\partial_x\psi\rangle = \iint \mathrm{d}A_F(ikx_F)\psi\left(x_F, y_F; \mathbf{x}\right)|x_F, y_F\rangle\,, \tag{S6a}$$

$$|\partial_y\psi\rangle = \iint \mathrm{d}A_F(iky_F)\psi\left(x_F, y_F; \mathbf{x}\right)|x_F, y_F\rangle\,, \tag{S6b}$$

$$|\partial_z\psi\rangle = \iint \mathrm{d}A_F\left(ik\sqrt{1-r_F^2}\right)\psi\left(x_F, y_F; \mathbf{x}\right)|x_F, y_F\rangle\,. \tag{S6c}$$

We seek an orthonormal basis $\mathscr{B}$ for the Hilbert space spanned by $|\psi\rangle$, $|\partial_x\psi\rangle$, $|\partial_y\psi\rangle$, and $|\partial_z\psi\rangle$. Note that elements of $\{|\psi\rangle, |\partial_x\psi\rangle, |\partial_y\psi\rangle\}$ are mutually orthogonal, as the relevant overlap integrals each have integrands that are odd functions of $x_F$ and/or $y_F$. The latter two need only to be normalized. We evaluate the norm of $|\partial_x\psi\rangle$:

$$\begin{aligned}\langle\partial_x\psi|\partial_x\psi\rangle &= k^2\mathcal{A}^2\iint \mathrm{d}A_F\frac{x_F^2}{\sqrt{1-r_F^2}}\mathrm{Circ}\left(\frac{nr_F}{\mathrm{NA}}\right)\\ &= k^2\mathcal{A}^2\int_0^{\mathrm{NA}/n} r_F\mathrm{d}r_F\int_0^{2\pi}\mathrm{d}\varphi_F\frac{r_F^2\cos^2\varphi_F}{\sqrt{1-r_F^2}}\\ &= \frac{\pi k^2\mathcal{A}^2}{3}\left[2-\left(2+(\mathrm{NA}/n)^2\right)\sqrt{1-(\mathrm{NA}/n)^2}\right].\end{aligned} \tag{S7}$$

One can show that $\langle\partial_y\psi|\partial_y\psi\rangle = \langle\partial_x\psi|\partial_x\psi\rangle$. Define

$$C_{xy} = \frac{1}{\sqrt{\langle\partial_x\psi|\partial_x\psi\rangle}} = \frac{1}{\sqrt{\langle\partial_y\psi|\partial_y\psi\rangle}}, \tag{S8}$$

and

$$|\psi_x\rangle = C_{xy}\,|\partial_x\psi\rangle\,, \tag{S9a}$$

$$|\psi_y\rangle = C_{xy}\,|\partial_y\psi\rangle\,. \tag{S9b}$$

Now $\{|\psi\rangle, |\psi_x\rangle, |\psi_y\rangle\}$ is orthonormal. One more basis vector must be added to construct $\mathscr{B}$ such that it includes $|\partial_z\psi\rangle$ in its span. We have $\langle\psi_x|\partial_z\psi\rangle = \langle\psi_y|\partial_z\psi\rangle = 0$ since again these overlap integrals have integrands that are odd functions of $x_F$ and $y_F$, respectively. However, $\gamma \equiv \langle\psi|\partial_z\psi\rangle \neq 0$. In fact we can evaluate $\gamma$ analytically:

$$\begin{aligned}\gamma &= ik\mathcal{A}^2\iint \mathrm{d}A_F\mathrm{Circ}\left(\frac{nr_F}{\mathrm{NA}}\right)\\ &= ik\mathcal{A}^2\pi(\mathrm{NA}/n)^2.\end{aligned} \tag{S10}$$

Letting

$$C_z = \frac{1}{\sqrt{\langle \partial_z \psi | \partial_z \psi \rangle}} = \frac{\sqrt{3}}{k\mathcal{A}\sqrt{2\pi}} \left[ 1 - \left( 1 - (\mathrm{NA}/n)^2 \right)^{3/2} \right]^{-1/2}, \tag{S11}$$

we can proceed by the Gram-Schmidt algorithm to obtain:

$$|\psi_z\rangle = \frac{|\partial_z \psi\rangle - \gamma |\psi\rangle}{\sqrt{C_z^{-2} - |\gamma|^2}}. \tag{S12}$$

The result is the orthonormal basis $\mathscr{B} = \{|\psi\rangle, |\psi_x\rangle, |\psi_y\rangle, |\psi_z\rangle\}$. The operators of the LHS of Eq. (S4) can be expressed:

$$\partial_x \rho = \frac{1}{C_{xy}} \Big( |\psi\rangle \langle \psi_x| + |\psi_x\rangle \langle \psi| \Big), \tag{S13a}$$

$$\partial_y \rho = \frac{1}{C_{xy}} \Big( |\psi\rangle \langle \psi_y| + |\psi_y\rangle \langle \psi| \Big), \tag{S13b}$$

$$\partial_z \rho = \sqrt{C_z^{-2} - |\gamma|^2} \Big( |\psi\rangle \langle \psi_z| + |\psi_z\rangle \langle \psi| \Big). \tag{S13c}$$

The SLDs can now be computed directly from Eqs. (S5) and (S48) to give:

$$\mathcal{L}_x = \frac{2}{C_{xy}} \Big( |\psi\rangle \langle \psi_x| + |\psi_x\rangle \langle \psi| \Big), \tag{S14a}$$

$$\mathcal{L}_y = \frac{2}{C_{xy}} \Big( |\psi\rangle \langle \psi_y| + |\psi_y\rangle \langle \psi| \Big), \tag{S14b}$$

$$\mathcal{L}_z = 2\sqrt{C_z^{-2} - |\gamma|^2} \Big( |\psi\rangle \langle \psi_z| + |\psi_z\rangle \langle \psi| \Big). \tag{S14c}$$

The elements of the quantum Fisher information matrix $\mathcal{K}$ can be computed according to:

$$\mathcal{K}_{ij} = \frac{1}{2} \mathrm{Re\ Tr}\ \rho \left( \mathcal{L}_{x_i} \mathcal{L}_{x_j} + \mathcal{L}_{x_j} \mathcal{L}_{x_i} \right), \tag{S15}$$

yielding the result:

$$\mathcal{K} = 4 \begin{pmatrix} C_{xy}^{-2} & 0 & 0 \\ 0 & C_{xy}^{-2} & 0 \\ 0 & 0 & C_z^{-2} - |\gamma|^2 \end{pmatrix}. \tag{S16}$$

The quantum precision bounds for each dimension are given simply by the inverse square roots of the diagonal elements in Eq. (S16):

$$\sigma_x^{(\mathrm{QCRB})} = C_{xy}/2, \tag{S17a}$$

$$\sigma_y^{(\mathrm{QCRB})} = C_{xy}/2, \tag{S17b}$$

$$\sigma_z^{(\mathrm{QCRB})} = \left(C_z^{-2} - |\gamma|^2\right)^{-1/2}/2. \tag{S17c}$$

As mentioned in the main text, necessary and sufficient conditions for the existence of a measurement that simultaneously saturates the QCRB in each dimension are in fact met here [10–12]. First, the Fisher information matrix $\mathcal{K}$ is diagonal, as seen in Eq. (S16). Second, the condition $\mathrm{Tr}\left(\rho\left[\mathcal{L}_x, \mathcal{L}_y\right]\right) = \mathrm{Tr}\left(\rho\left[\mathcal{L}_y, \mathcal{L}_z\right]\right) = \mathrm{Tr}\left(\rho\left[\mathcal{L}_z, \mathcal{L}_x\right]\right) = 0$ is met, where $\{\mathcal{L}_x, \mathcal{L}_y, \mathcal{L}_z\}$ are defined in Eq. (S14) and $\rho = |\psi\rangle\langle\psi|$. These two conditions ensure the existence of such a measurement. However, we note that the choice of SLDs given in Eq. (S14) do not in fact commute, and so a measurement that simultaneously projects onto the eigenbasis of each of these is not possible.

## III. ON THE EIGENSTATES OF THE SINGLE-OBJECTIVE $\mathcal{L}_z$

In this work we present a variant of a radial shear interferometer that numerically approaches the QCRB with respect to $z$ estimation in the case of single-objective collection. As mentioned, a sufficient condition to saturate the QCRB of a single parameter is for a measurement to project onto the eigenbasis of the corresponding SLD, in this case $\mathcal{L}_z$ [13] . Here we describe the relation between the radial shear interferometer and such a projection measurement.

In Section II we show that $\mathcal{L}_z$ can be expressed:

$$\mathcal{L}_z = 2\sqrt{C_z^{-2} - |\gamma|^2}\left(|\psi\rangle\langle\psi_z| + |\psi_z\rangle\langle\psi|\right), \tag{S18}$$

with $C_z$, $\gamma$, and $|\psi_z\rangle$ defined in Eqs. (S10), (S11), and (S12), respectively. $\mathcal{L}_z$ has eigenstates $|\Phi_+\rangle$ and $|\Phi_-\rangle$ defined by:

$$|\Phi_+\rangle = \frac{1}{\sqrt{2}}\left(|\psi\rangle + |\psi_z\rangle\right), \tag{S19a}$$

$$|\Phi_-\rangle = \frac{1}{\sqrt{2}}\left(|\psi\rangle - |\psi_z\rangle\right). \tag{S19b}$$

With a little algebra we can write:

$$|\Phi_+\rangle = \iint \mathrm{d}A_F \Phi_+ (x_F, y_F) \, |x_F, y_F\rangle \,, \tag{S20a}$$

$$|\Phi_-\rangle = \iint \mathrm{d}A_F \Phi_- (x_F, y_F) \, |x_F, y_F\rangle \,, \tag{S20b}$$

where the classical wavefunctions $\Phi_+ (x_F, y_F)$ and $\Phi_- (x_F, y_F)$ are defined by:

$$\Phi_+ (x_F, y_F) = \frac{1}{\sqrt{2}} \left( 1 + \frac{ik\sqrt{1 - r_F^2} - \gamma}{\sqrt{C_Z^{-2} - |\gamma|^2}} \right) \psi (x_F, y_F) \,, \tag{S21a}$$

$$\Phi_- (x_F, y_F) = \frac{1}{\sqrt{2}} \left( 1 - \frac{ik\sqrt{1 - r_F^2} - \gamma}{\sqrt{C_Z^{-2} - |\gamma|^2}} \right) \psi (x_F, y_F) \,. \tag{S21b}$$

Note that since $\psi(x_F, y_F)$ depends implicitly on $z$, so too do $\Phi_+(x_F, y_F)$ and $\Phi_-(x_F, y_F)$. A measurement that produces the desired projections for a particular choice of $z$ is only guaranteed to achieve the QCRB in a region near that $z$, a microcosm of a more general phenomenon in quantum parameter estimation in which the optimality of the measurement often depends on the state itself [14]. Figure S5 depicts both the intensity and phase functions associated with $\Phi_+ (x_F, y_F)$ and $\Phi_- (x_F, y_F)$ for $z = 0$. To determine how the operation of the radial shear interferometer compares to the projection operators $\{|\Phi_+\rangle \langle\Phi_+| \,, |\Phi_-\rangle \langle\Phi_-|\}$ we compute the diffraction integrals described in Section IV with both $\Phi_+ (x_F, y_F)$ and $\Phi_- (x_F, y_F)$ as inputs. The results are illustrated in Fig. S5. We find that when $|\Phi_+\rangle$ is input to our interferometer the vast majority of the light is shunted to detector 2, while inputting $|\Phi_-\rangle$ results in the majority of signal falling on detector 1. In effect we see that our radial shear interferometer approximates projection on the eigenstates of $\mathcal{L}_z$. The fact that the approximation is not exact is consistent with the fact that the CRB attained by the interferometer as presently parameterized is actually slightly greater than the QCRB. As mentioned elsewhere in this work, the approximation can be further improved by adding arms to the interferometer that employ the unused inner ring of light.

## IV. DETAILS FOR RADIAL SHEAR INTERFEROMETER

In this section we describe the radial shear interferometer setup in greater detail, giving specifications and describing the diffraction integrals computed in simulating the measure-

ment. Figure S3 shows schematics of the inner and outer arms of the interferometer, unfolded for clarity and with exact distances indicated.

In the main text we define the wavefunction at the Fourier plane at the back aperture of the objective lens by

$$\psi(x_F, y_F) = \mathcal{A}\left(1 - r_F^2\right)^{-1/4} \mathrm{Circ}\left(\frac{n r_F}{\mathrm{NA}}\right) \exp\left[ik\left(x x_F + y y_F + z\sqrt{1 - r_F^2}\right)\right], \tag{S22}$$

where the spatial coordinates $x_F$, $y_F$, and $r_F = \sqrt{x_F^2 + y_F^2}$ are scaled such that the support of $\psi(x_F, y_F)$ is $r_F \leq \mathrm{NA}/n$. As discussed in the main text, what we mean by this formalism is that the light is in a statistical state with normalized Fourier-plane mutual coherence function $g(x_F, y_F, x'_F, y'_F) = \psi(x_F, y_F)\psi^*(x'_F, y'_F)$. We can obtain the normalized mutual coherence function at the detectors by propagating $\psi(x_F, y_F)$ to the detector planes via the ordinary rules of linear optics, then taking the analogous outer product.

Invoking the Abbe sine condition, at the back aperture of the microscope objective we can relate the scaled coordinates in Eq. (S22) to unscaled coordinates $\tilde{x}_F$, $\tilde{y}_F$, and $\tilde{r}_F$ via:

$$\tilde{x}_F = \frac{n f_{\mathrm{TL}}}{\sqrt{M_{\mathrm{sys}}^2 - \mathrm{NA}^2}} x_F, \tag{S23a}$$

$$\tilde{y}_F = \frac{n f_{\mathrm{TL}}}{\sqrt{M_{\mathrm{sys}}^2 - \mathrm{NA}^2}} y_F, \tag{S23b}$$

$$\tilde{r}_F = \frac{n f_{\mathrm{TL}}}{\sqrt{M_{\mathrm{sys}}^2 - \mathrm{NA}^2}} r_F, \tag{S23c}$$

where $f_{\mathrm{TL}}$ is the focal length of the tube lens and $M_{\mathrm{sys}}$ is the magnification of the objective-tube lens unit (i.e., the magnification written on the objective casing, assuming the company-intended tube lens is used). For our purposes we assume $M_{\mathrm{sys}} = 100$ and $f_{\mathrm{TL}} = 180$ mm, the latter of which is the standard for Olympus microscopes. For such a system magnification we can approximate $\sqrt{M_{\mathrm{sys}}^2 - \mathrm{NA}^2} \approx M_{\mathrm{sys}}$ such that the unscaled coordinates can be redefined more simply:

$$\tilde{x}_F = \frac{n f_{\mathrm{TL}}}{M_{\mathrm{sys}}} x_F, \tag{S24a}$$

$$\tilde{y}_F = \frac{n f_{\mathrm{TL}}}{M_{\mathrm{sys}}} y_F, \tag{S24b}$$

$$\tilde{r}_F = \frac{n f_{\mathrm{TL}}}{M_{\mathrm{sys}}} r_F. \tag{S24c}$$

As designed, the second lens after the objective (the first after the tube lens) has focal length $f = 200$ mm. Thus the coordinates at the second conjugate Fourier plane (formed at the SLM plane) must be scaled by an additional magnification factor equal to $f/f_{\mathrm{TL}}$. In the main text we describe imparting a small amount of defocus with the SLM at a conjugate Fourier plane before the annular mirror in order to compensate for defocus accrued downstream. A defocus equivalent to $\Delta z = 73$ nm approximately achieves this goal for the arrangement depicted in Fig. S3. In practice $\Delta z$ can be modulated to feed back on the position of a tracked emitter. The wavefunction at the conjugate Fourier plane just before the annular mirror, as a function of unscaled coordinates, can then be defined:

$$\tilde{\psi}\left(\tilde{x}_F, \tilde{y}_F\right) = \left(\frac{M_{\mathrm{sys}}}{nf}\right) \psi\left(\frac{M_{\mathrm{sys}}}{nf}\tilde{x}_F, \frac{M_{\mathrm{sys}}}{nf}\tilde{y}_F\right) \exp\left[ik\Delta z\sqrt{1-\left(\frac{M_{\mathrm{sys}}}{nf}\tilde{r}_F\right)^2}\right], \tag{S25}$$

where the prefactor ensures $\iint \mathrm{d}\tilde{x}_F \mathrm{d}\tilde{y}_F |\tilde{\psi}\left(\tilde{x}_F, \tilde{y}_F\right)|^2 = 1$.

We will now carry out the transformation of $\tilde{\psi}\left(\tilde{x}_F, \tilde{y}_F\right)$ through the inner arm of the interferometer [Fig. S3(a)]. As described in the main text, the inner radius of the annular mirror (in scaled units) is $r_\circ = 0.6326$, such that the wavefunction in the inner arm just after the annular mirror is:

$$\psi^{(\mathrm{i})}\left(x^{(\mathrm{i})}, y^{(\mathrm{i})}\right) = \tilde{\psi}\left(x^{(\mathrm{i})}, y^{(\mathrm{i})}\right) \mathrm{Circ}\left(\frac{M_{\mathrm{sys}}}{nfr_\circ} r^{(\mathrm{i})}\right), \tag{S26}$$

where $x^{(\mathrm{i})}$, $y^{(\mathrm{i})}$, and $r^{(\mathrm{i})} = \sqrt{(x^{(\mathrm{i})})^2 + (y^{(\mathrm{i})})^2}$ are the coordinates defined in this plane.

The lenses labeled $\mathrm{L}_i$ for $i \in \{1, 2, 3, 4, 5\}$ in Fig. S3(a) have a common focal length of $f = 200$ mm. A second type of lens labeled $\mathrm{L}'$ in Fig. S3(a) has a shorter focal length of $f' = 44$ mm, chosen such that the the wavefunction at the back focal plane of $\mathrm{L}'$ is demagnified by a factor $M = f'/f = 0.22$. At this plane, just before the first axicon lens ($\mathrm{A}_+$), the wavefunction is:

$$\psi^{(\mathrm{ii})}\left(x^{(\mathrm{ii})}, y^{(\mathrm{ii})}\right) = -\frac{1}{M}\psi^{(\mathrm{i})}\left(\frac{x^{(\mathrm{ii})}}{M}, -\frac{y^{(\mathrm{ii})}}{M}\right), \tag{S27}$$

where the signs of the arguments result from an inversion and a reflection during propagation. As described in the main text, the axicon $\mathrm{A}_+$ imparts a phase delay proportional to distance from the optical axis. We heuristically choose a proportionality constant such that the wavefunction just after $\mathrm{A}_+$ is given by:

$$\psi^{(\mathrm{iii})}\left(x^{(\mathrm{iii})}, y^{(\mathrm{iii})}\right) = \psi^{(\mathrm{ii})}\left(x^{(\mathrm{iii})}, y^{(\mathrm{iii})}\right) \exp\left[\frac{680iM_{\mathrm{sys}}}{nf} r^{(\mathrm{iii})}\right]. \tag{S28}$$

As an aside, we here consider the implication of Eq. (S28) on the inclination angle $\Theta$ labeled in Fig. S3(a). Assuming the axicon is made of glass with index of refraction $n = 1.518$ (i.e., equal to that of the objective immersion oil), one can deduce from geometry:

$$\Theta = \arctan\left(\frac{680\lambda_\circ M_{\text{sys}}}{2\pi(n-1)nf}\right) \approx 2.6^\circ. \tag{S29}$$

Next we seek an expression for the wavefunction after propagation from the axicon $\text{A}_+$ to the back focal plane of lens $\text{L}_2$. This can be obtained as a scaled Fourier transform multiplied by a quadratic phase factor [15]:

$$\begin{aligned}\psi^{(\text{iv})}\left(x^{(\text{iv})}, y^{(\text{iv})}\right) =& \frac{\exp\left(-\frac{i\pi}{2\lambda_\circ f}\left[(x^{(\text{iv})})^2 + (y^{(\text{iv})})^2\right]\right)}{i\lambda_\circ f} \\ & \times \iint \mathrm{d}x^{(\text{iii})}\mathrm{d}y^{(\text{iii})}\psi^{(\text{iii})}\left(x^{(\text{iii})}, y^{(\text{iii})}\right)\exp\left(-\frac{2\pi i}{\lambda_\circ f}\left[x^{(\text{iii})}x^{(\text{iv})} + y^{(\text{iii})}y^{(\text{iv})}\right]\right).\end{aligned} \tag{S30}$$

In practice we computed Eq. (S30) and subsequent diffraction integrals numerically via appropriate application of the MATLAB function fft2. Propagation to the back focal plane of lens $\text{L}_3$, just before the axicon $\text{A}_-$, gives the wavefunction:

$$\psi^{(\text{v})}\left(x^{(\text{v})}, y^{(\text{v})}\right) = \frac{1}{i\lambda_\circ f}\iint \mathrm{d}x^{(\text{iv})}\mathrm{d}y^{(\text{iv})}\psi^{(\text{iv})}\left(x^{(\text{iv})}, y^{(\text{iv})}\right)\exp\left(-\frac{2\pi i}{\lambda_\circ f}\left[x^{(\text{iv})}x^{(\text{v})} + y^{(\text{iv})}y^{(\text{v})}\right]\right). \tag{S31}$$

The axicon $\text{A}_-$ imparts a phase delay of opposite sign to that of $\text{A}_+$ such that just after $\text{A}_-$ we have:

$$\psi^{(\text{vi})}\left(x^{(\text{vi})}, y^{(\text{vi})}\right) = \psi^{(\text{v})}\left(x^{(\text{vi})}, y^{(\text{vi})}\right)\exp\left[-\frac{680iM_{\text{sys}}}{nf}r^{(\text{vi})}\right]. \tag{S32}$$

At the back focal plane of lens $\text{L}_4$ we have:

$$\begin{aligned}\psi^{(\text{vii})}\left(x^{(\text{vii})}, y^{(\text{vii})}\right) =& \frac{\exp\left(\frac{i\pi}{2\lambda_\circ f}\left[(x^{(\text{vii})})^2 + (y^{(\text{vii})})^2\right]\right)}{i\lambda_\circ f} \\ & \times \iint \mathrm{d}x^{(\text{vi})}\mathrm{d}y^{(\text{vi})}\psi^{(\text{vi})}\left(x^{(\text{vi})}, y^{(\text{vi})}\right)\exp\left(-\frac{2\pi i}{\lambda_\circ f}\left[x^{(\text{vi})}x^{(\text{vii})} + y^{(\text{vi})}y^{(\text{vii})}\right]\right),\end{aligned} \tag{S33}$$

and at the back focal plane of lens $\text{L}_5$:

$$\begin{aligned}\psi^{(\text{viii})}\left(x^{(\text{viii})}, y^{(\text{viii})}\right) =& \frac{1}{i\lambda_\circ f}\iint \mathrm{d}x^{(\text{vii})}\mathrm{d}y^{(\text{vii})}\psi^{(\text{vii})}\left(x^{(\text{vii})}, y^{(\text{vii})}\right) \\ & \times \exp\left(-\frac{2\pi i}{\lambda_\circ f}\left[x^{(\text{vii})}x^{(\text{viii})} + y^{(\text{vii})}y^{(\text{viii})}\right]\right).\end{aligned} \tag{S34}$$

Next we consider the transformations in the outer arm of the interferometer [Fig. S3(b)]. Just after the annular mirror the wavefunction in this arm is given simply by:

$$\psi^{(\mathrm{o})}\left(x^{(\mathrm{o})},y^{(\mathrm{o})}\right)=\tilde{\psi}\left(-x^{(\mathrm{o})},y^{(\mathrm{o})}\right)-\psi^{(\mathrm{i})}\left(-x^{(\mathrm{o})},y^{(\mathrm{o})}\right). \tag{S35}$$

Each lens $\mathrm{L}_j''$ for $j\in\{1,2,3,4\}$ in the outer arm has focal length $f''=261$ mm, chosen such that the total distance from annular mirror to beam splitter is the same as that in the inner arm (2.088 m). The lenses $\mathrm{L}_j''$ are arranged such that they form two sequential telescopes of unit magnification, effectively relaying $\psi^{(\mathrm{o})}$ to the beam splitter plane unchanged save for a reflection.

Finally, just after the beam splitter the wavefunctions in each of the output ports are given by:

$$\psi_1\left(x_1,y_1\right)=\frac{1}{\sqrt{2}}\Big[\psi^{(\mathrm{viii})}\left(x_1,y_1\right)+i\psi^{(\mathrm{o})}\left(x_1,y_1\right)\Big], \tag{S36a}$$

$$\psi_2\left(x_2,y_2\right)=\frac{1}{\sqrt{2}}\Big[i\psi^{(\mathrm{viii})}\left(-x_2,y_2\right)+\psi^{(\mathrm{o})}\left(-x_2,y_2\right)\Big]. \tag{S36b}$$

## V. DERIVATION OF DUAL-OBJECTIVE QCRB

Here we will derive the QFI and QCRB for localization with single-objective collection. Again we begin with the single-photon state $\rho=|\psi\rangle\langle\psi|$. However now $|\psi\rangle$ is distributed between coordinates localized to the back apertures of both objectives $a$ and $b$:

$$|\psi\rangle=\frac{1}{\sqrt{2}}\left(|\psi^{(a)}\rangle+|\psi^{(b)}\rangle\right), \tag{S37}$$

where

$$|\psi^{(a)}\rangle=\iint \mathrm{d}A_F^{(a)}\psi\left(x_F^{(a)},y_F^{(a)};[x,y,z]^{\mathrm{T}}\right)\left|x_F^{(a)},y_F^{(a)}\right\rangle, \tag{S38}$$

and

$$|\psi^{(b)}\rangle=\iint \mathrm{d}A_F^{(b)}\psi\left(x_F^{(b)},y_F^{(b)};[-x,y,-z]^{\mathrm{T}}\right)\left|x_F^{(b)},y_F^{(b)}\right\rangle. \tag{S39}$$

Here

$$\psi\left(x_F^{(a)},y_F^{(a)};[x,y,z]^{\mathrm{T}}\right)=\mathcal{A}\left(1-\left(r_F^{(a)}\right)^2\right)^{-1/4}\mathrm{Circ}\left(\frac{nr_F^{(a)}}{NA}\right)\times\exp\left[ik\left(xx_F^{(a)}+yy_F^{(a)}+z\sqrt{1-\left(r_F^{(a)}\right)^2}\right)\right], \tag{S40}$$

and

$$\psi\left(x_F^{(b)}, y_F^{(b)}; [-x, y, -z]^{\mathrm{T}}\right) = \mathcal{A}\left(1 - \left(r_F^{(b)}\right)^2\right)^{-1/4} \mathrm{Circ}\left(\frac{n r_F^{(b)}}{NA}\right) \times \exp\left[ik\left(-x x_F^{(b)} + y y_F^{(b)} - z\sqrt{1 - \left(r_F^{(b)}\right)^2}\right)\right]. \quad \text{(S41)}$$

As in the single-objective case, we seek to express the SLDs $\mathcal{L}_x$, $\mathcal{L}_y$, and $\mathcal{L}_z$. The unnormalized states $|\partial_x\psi\rangle$, $|\partial_y\psi\rangle$, and $|\partial_z\psi\rangle$ are now given by:

$$|\partial_x\psi\rangle = \frac{ik}{\sqrt{2}}\left[\iint \mathrm{d}A_F^{(a)} x_F^{(a)} \psi\left(x_F^{(a)}, y_F^{(a)}; [x, y, z]^{\mathrm{T}}\right)\left|x_F^{(a)}, y_F^{(a)}\right\rangle - \iint \mathrm{d}A_F^{(b)} x_F^{(b)} \psi\left(x_F^{(b)}, y_F^{(b)}; [-x, y, -z]^{\mathrm{T}}\right)\left|x_F^{(b)}, y_F^{(b)}\right\rangle\right], \quad \text{(S42a)}$$

$$|\partial_y\psi\rangle = \frac{ik}{\sqrt{2}}\left[\iint \mathrm{d}A_F^{(a)} y_F^{(a)} \psi\left(x_F^{(a)}, y_F^{(a)}; [x, y, z]^{\mathrm{T}}\right)\left|x_F^{(a)}, y_F^{(a)}\right\rangle + \iint \mathrm{d}A_F^{(b)} y_F^{(b)} \psi\left(x_F^{(b)}, y_F^{(b)}; [-x, y, -z]^{\mathrm{T}}\right)\left|x_F^{(b)}, y_F^{(b)}\right\rangle\right], \quad \text{(S42b)}$$

$$|\partial_z\psi\rangle = \frac{ik}{\sqrt{2}}\left[\iint \mathrm{d}A_F^{(a)} \sqrt{1 - \left(r_F^{(a)}\right)^2} \psi\left(x_F^{(a)}, y_F^{(a)}; [x, y, z]^{\mathrm{T}}\right)\left|x_F^{(a)}, y_F^{(a)}\right\rangle - \iint \mathrm{d}A_F^{(b)} \sqrt{1 - \left(r_F^{(b)}\right)^2} \psi\left(x_F^{(b)}, y_F^{(b)}; [-x, y, -z]^{\mathrm{T}}\right)\left|x_F^{(b)}, y_F^{(b)}\right\rangle\right]. \quad \text{(S42c)}$$

We seek an orthonormal basis $\mathscr{B}$ for the Hilbert space spanned by $|\psi\rangle$, $|\partial_x\psi\rangle$, $|\partial_y\psi\rangle$, and $|\partial_z\psi\rangle$. The fact that $\left\langle x_F^{(a)}, y_F^{(a)} \middle| x_F^{(b)}, y_F^{(b)} \right\rangle = 0$ means we can ignore cross terms in evaluating the overlap integrals. As in the single-objective case we can quickly conclude that each of $\{|\psi\rangle, |\partial_x\psi\rangle, |\partial_y\psi\rangle\}$ are mutually orthogonal as the associated integrals all have integrands that are odd functions of $x_F$ and/or $y_F$. Also note that the norms of the derivative states are the same as those of their counterparts in the single-objective case. That is,

$$\langle\partial_x\psi|\partial_x\psi\rangle = 1/C_{xy}^2, \quad \text{(S43a)}$$

$$\langle\partial_y\psi|\partial_y\psi\rangle = 1/C_{xy}^2, \quad \text{(S43b)}$$

$$\langle\partial_z\psi|\partial_z\psi\rangle = 1/C_z^2, \quad \text{(S43c)}$$

where $C_{xy}$ and $C_z$ are exactly as they are defined in the main text. Again defining

$$|\psi_x\rangle = C_{xy}|\partial_x\psi\rangle, \quad \text{(S44a)}$$

$$|\psi_y\rangle = C_{xy}|\partial_y\psi\rangle, \quad \text{(S44b)}$$

we obtain the orthonormal set $\{|\psi\rangle, |\psi_x\rangle, |\psi_y\rangle\}$. Yet again we have $\langle\psi_x|\partial_z\psi\rangle = \langle\psi_y|\partial_z\psi\rangle = 0$ since these integrals too are odd functions of $x_F$ and $y_F$, respectively. However, unlike in the single-objective case, we also have $\langle\psi|\partial_z\psi\rangle = 0$:

$$\begin{aligned}\langle\psi|\partial_z\psi\rangle = \frac{k^2}{2}\Bigg[&\iint \mathrm{d}A_F^{(a)}\sqrt{1-\left(r_F^{(a)}\right)^2}\left|\psi\left(x_F^{(a)}, y_F^{(a)}\right)\right|^2 \\ &- \iint \mathrm{d}A_F^{(b)}\sqrt{1-\left(r_F^{(b)}\right)^2}\left|\psi\left(x_F^{(b)}, y_F^{(b)}\right)\right|^2\Bigg] \\ &= 0, \end{aligned} \tag{S45}$$

where in the second line we recognize that the two terms are of equal absolute value and opposite sign. Hence, in contrast to the single-objective case, we define

$$|\psi_z\rangle = C_z\,|\partial_z\psi\rangle \tag{S46}$$

in the dual-objective case, and obtain the desired orthonormal basis $\mathscr{B} = \{|\psi\rangle, |\psi_x\rangle, |\psi_y\rangle, |\psi_z\rangle\}$. We can write:

$$\partial_x\rho = \frac{1}{C_{xy}}\Big(\,|\psi\rangle\langle\psi_x| + |\psi_x\rangle\langle\psi|\,\Big), \tag{S47a}$$

$$\partial_y\rho = \frac{1}{C_{xy}}\Big(\,|\psi\rangle\langle\psi_y| + |\psi_y\rangle\langle\psi|\,\Big), \tag{S47b}$$

$$\partial_z\rho = \frac{1}{C_z}\Big(\,|\psi\rangle\langle\psi_z| + |\psi_z\rangle\langle\psi|\,\Big). \tag{S47c}$$

The SLDs are given by:

$$\mathcal{L}_x = \frac{2}{C_{xy}}\Big(\,|\psi\rangle\langle\psi_x| + |\psi_x\rangle\langle\psi|\,\Big), \tag{S48a}$$

$$\mathcal{L}_y = \frac{2}{C_{xy}}\Big(\,|\psi\rangle\langle\psi_y| + |\psi_y\rangle\langle\psi|\,\Big), \tag{S48b}$$

$$\mathcal{L}_z = \frac{2}{C_z}\Big(\,|\psi\rangle\langle\psi_z| + |\psi_z\rangle\langle\psi|\,\Big). \tag{S48c}$$

Computing the elements of the quantum Fisher information matrix $\mathcal{K}$ according to

$$\mathcal{K}_{ij} = \frac{1}{2}\mathrm{Re\ Tr}\ \rho\left(\mathcal{L}_{x_i}\mathcal{L}_{x_j} + \mathcal{L}_{x_j}\mathcal{L}_{x_i}\right), \tag{S49}$$

yields the result

$$\mathcal{K} = 4\begin{pmatrix} C_{xy}^{-2} & 0 & 0 \\ 0 & C_{xy}^{-2} & 0 \\ 0 & 0 & C_z^{-2} \end{pmatrix}. \tag{S50}$$

The quantum precision bounds for each dimension are given simply by the inverse square roots of the diagonal elements in Eq. (S50):

$$\sigma_x^{(\mathrm{QCRB})} = C_{xy}/2, \tag{S51a}$$

$$\sigma_y^{(\mathrm{QCRB})} = C_{xy}/2, \tag{S51b}$$

$$\sigma_z^{(\mathrm{QCRB})} = C_z/2. \tag{S51c}$$

Yet again we see that $\mathcal{K}$ is diagonal, and that $\mathrm{Tr}\left(\rho\left[\mathcal{L}_i, \mathcal{L}_j\right]\right) = 0$, $\forall i \neq j$ with $i, j \in \{x, y, z\}$. Thus, again we find that necessary and sufficient conditions for the existence of a measurement that simultaneously saturates the QCRB of each parameter simultaneously are met [10]. This of course must be true since we have identified such a measurement in inteferometric dual-objective detection. We give further insight in the section below.

## VI. ON THE OPTIMALITY OF INTERFEROMETRIC DUAL-OBJECTIVE DETECTION

Our goal in this section is to give additional insight into the optimality of dual-objective interferometric detection. To simplify the mathematics, consider the variant of interferometric dual-objective detection sketched in Fig. S7(a), in which the detectors are placed at conjugate Fourier planes rather than image planes. As seen in Fig. S7(b,c), this arrangement also saturates the QCRB of each parameter simultaneously.

Reference [11] details properties of a projection measurement that simultaneously saturates multiparameter QCRBs for a pure input state. These properties should coincide with our case in which we ignore contributions from multiphoton terms and equate the QFI with that of the associated pure state. By inspection, the measurement in Fig. S7 can be mapped to a set of projectors $\left\{ \left|\Upsilon_1\left(x_1, y_1\right)\right\rangle \left\langle\Upsilon_1\left(x_1, y_1\right)\right|, \left|\Upsilon_2\left(x_2, y_2\right)\right\rangle \left\langle\Upsilon_2\left(x_2, y_2\right)\right| \right\}$, where $(x_1, y_1)$ and $(x_2, y_2)$ are defined on their supports at both output ports of the beam splitter. The

states $|\Upsilon_1(x_1,y_1)\rangle$ and $|\Upsilon_2(x_2,y_2)\rangle$ are given by:

$$|\Upsilon_1(x_1,y_1)\rangle = \frac{1}{\sqrt{2}}\left[-i\iint \mathrm{d}A_F^{(a)}\delta\left(x_F^{(a)}-x_1,y_F^{(a)}-y_1\right)\left|x_F^{(a)},y_F^{(a)}\right\rangle + \iint \mathrm{d}A_F^{(b)}\delta\left(x_F^{(b)}-x_1,y_F^{(b)}+y_1\right)\left|x_F^{(b)},y_F^{(b)}\right\rangle\right], \tag{S52a}$$

$$|\Upsilon_2(x_2,y_2)\rangle = \frac{1}{\sqrt{2}}\left[\iint \mathrm{d}A_F^{(a)}\delta\left(x_F^{(a)}+x_2,y_F^{(a)}-y_2\right)\left|x_F^{(a)},y_F^{(a)}\right\rangle - i\iint \mathrm{d}A_F^{(b)}\delta\left(x_F^{(b)}+x_2,y_F^{(b)}+y_2\right)\left|x_F^{(b)},y_F^{(b)}\right\rangle\right]. \tag{S52b}$$

One can show that indeed the projectors $\left\{|\Upsilon_1(x_1,y_1)\rangle\langle\Upsilon_1(x_1,y_1)|, |\Upsilon_2(x_2,y_2)\rangle\langle\Upsilon_2(x_2,y_2)|\right\}$ meet the requirements outlined in [11] for a measurement that reaches the multiparameter QCRB.

Even more directly we can compute the classical Fisher information matrix $\mathcal{J}$ analytically and show that in this case $\mathcal{J}=\mathcal{K}$. As a function of appropriately scaled coordinates $(x_1,y_1)$ at output port 1, the portion of the wavefunction at this plane is given by:

$$\psi_1\left(x_1,y_1;[x,y,z]^{\mathrm{T}}\right) = \frac{i}{2}\psi\left(x_1,y_1;[x,y,z]^{\mathrm{T}}\right) + \frac{1}{2}\psi\left(x_1,-y_1;[-x,y,-z]^{\mathrm{T}}\right). \tag{S53}$$

Likewise, the portion with support at output port 2 is given by:

$$\psi_2\left(x_2,y_2;[x,y,z]^{\mathrm{T}}\right) = \frac{1}{2}\psi\left(-x_2,y_2;[x,y,z]^{\mathrm{T}}\right) + \frac{i}{2}\psi\left(-x_2,-y_2;[-x,y,-z]^{\mathrm{T}}\right). \tag{S54}$$

Note the normalization condition is $\iint \mathrm{d}A_1\left|\psi_1(x_1,y_1)\right|^2 + \iint \mathrm{d}A_2\left|\psi_2(x_2,y_2)\right|^2 = 1$. Define the phase function:

$$\theta\left(u,v;[x,y,z]^{\mathrm{T}}\right) \equiv k\left(xu+yv+z\sqrt{1-u^2-v^2}\right). \tag{S55}$$

Some algebra gives the relations:

$$\psi_1\left(x_1,y_1;[x,y,z]^{\mathrm{T}}\right) = \mathcal{A}\left(1-r_1^2\right)^{-1/4}\mathrm{Circ}\left(\frac{nr_1}{\mathrm{NA}}\right)e^{i\pi/4}\cos\left[\theta\left(x_1,y_1;[x,y,z]^{\mathrm{T}}\right)+\pi/4\right], \tag{S56a}$$

$$\psi_2\left(x_2,y_2;[x,y,z]^{\mathrm{T}}\right) = \mathcal{A}\left(1-r_2^2\right)^{-1/4}\mathrm{Circ}\left(\frac{nr_2}{\mathrm{NA}}\right)e^{i\pi/4}\cos\left[\theta\left(-x_2,y_2;[x,y,z]^{\mathrm{T}}\right)-\pi/4\right]. \tag{S56b}$$

Ignoring the extra inversion after the beam splitter since this will have no effect on $\mathcal{J}$, the intensity functions at each detector plane are then given by

$$\bar{I}_1\left(x_1, y_1; [x, y, z]^{\mathrm{T}}\right) = \left|\psi_1\left(x_1, y_1; [x, y, z]^{\mathrm{T}}\right)\right|^2, \tag{S57a}$$

$$\bar{I}_2\left(x_2, y_2; [x, y, z]^{\mathrm{T}}\right) = \left|\psi_2\left(x_2, y_2; [x, y, z]^{\mathrm{T}}\right)\right|^2, \tag{S57b}$$

yielding expressions:

$$\bar{I}_1\left(x_1, y_1; [x, y, z]^{\mathrm{T}}\right) = \frac{\mathcal{A}^2}{\sqrt{1-r_1^2}}\mathrm{Circ}\left(\frac{nr_1}{\mathrm{NA}}\right)\cos^2\left[\theta\left(x_1, y_1; [x, y, z]^{\mathrm{T}}\right) + \pi/4\right], \tag{S58a}$$

$$\bar{I}_2\left(x_2, y_2; [x, y, z]^{\mathrm{T}}\right) = \frac{\mathcal{A}^2}{\sqrt{1-r_2^2}}\mathrm{Circ}\left(\frac{nr_2}{\mathrm{NA}}\right)\cos^2\left[\theta\left(-x_2, y_2; [x, y, z]^{\mathrm{T}}\right) - \pi/4\right]. \tag{S58b}$$

The total classical Fisher information function $\mathcal{J}_{ij}$ is given by:

$$\mathcal{J}_{ij} = \iint \mathrm{d}A_1 \mathcal{J}_{ij}^{(1)}\left(x_1, y_1; [x, y, z]^{\mathrm{T}}\right) + \iint \mathrm{d}A_2 \mathcal{J}_{ij}^{(2)}\left(x_2, y_2; [x, y, z]^{\mathrm{T}}\right). \tag{S59}$$

The integrands in Eq. (S59) are given by:

$$\mathcal{J}_{ij}^{(1)}\left(x_1, y_1; [x, y, z]^{\mathrm{T}}\right) = \mathrm{Circ}\left(\frac{nr_1}{\mathrm{NA}}\right)\frac{\left[\partial_i \bar{I}_1\left(x_1, y_1; [x, y, z]^{\mathrm{T}}\right)\right]\left[\partial_j \bar{I}_1\left(x_1, y_1; [x, y, z]^{\mathrm{T}}\right)\right]}{\bar{I}_1\left(x_1, y_1; [x, y, z]^{\mathrm{T}}\right)}, \tag{S60a}$$

$$\mathcal{J}_{ij}^{(2)}\left(x_2, y_2; [x, y, z]^{\mathrm{T}}\right) = \mathrm{Circ}\left(\frac{nr_2}{\mathrm{NA}}\right)\frac{\left[\partial_i \bar{I}_2\left(x_2, y_2; [x, y, z]^{\mathrm{T}}\right)\right]\left[\partial_j \bar{I}_2\left(x_2, y_2; [x, y, z]^{\mathrm{T}}\right)\right]}{\bar{I}_2\left(x_2, y_2; [x, y, z]^{\mathrm{T}}\right)}. \tag{S60b}$$

Plugging Eq. (S58) into Eq. (S60) gives the expressions:

$$\begin{aligned}\mathcal{J}_{ij}^{(1)}\left(x_1, y_1; [x, y, z]^{\mathrm{T}}\right) = {} & \frac{2\mathcal{A}^2}{\sqrt{1-r_1^2}}\mathrm{Circ}\left(\frac{nr_1}{\mathrm{NA}}\right)\left(1 + \sin\left[2\theta\left(x_1, y_1; [x, y, z]^{\mathrm{T}}\right)\right]\right) \\ & \times \left[\partial_i \theta\left(x_1, y_1; [x, y, z]^{\mathrm{T}}\right)\right]\left[\partial_j \theta\left(x_1, y_1; [x, y, z]^{\mathrm{T}}\right)\right],\end{aligned} \tag{S61a}$$

$$\begin{aligned}\mathcal{J}_{ij}^{(2)}\left(x_2, y_2; [x, y, z]^{\mathrm{T}}\right) = {} & \frac{2\mathcal{A}^2}{\sqrt{1-r_2^2}}\mathrm{Circ}\left(\frac{nr_2}{\mathrm{NA}}\right)\left(1 - \sin\left[2\theta\left(-x_2, y_2; [x, y, z]^{\mathrm{T}}\right)\right]\right) \\ & \times \left[\partial_i \theta\left(-x_2, y_2; [x, y, z]^{\mathrm{T}}\right)\right]\left[\partial_j \theta\left(-x_2, y_2; [x, y, z]^{\mathrm{T}}\right)\right].\end{aligned} \tag{S61b}$$

Using the substitution $x_2' = -x_2$ we can rewrite the second integral in Eq. (S59):

$$\mathcal{J}_{ij} = \iint \mathrm{d}x_1 \mathrm{d}y_1 \mathcal{J}_{ij}^{(1)}\left(x_1, y_1; [x, y, z]^{\mathrm{T}}\right) + \iint \mathrm{d}x_2' \mathrm{d}y_2 \mathcal{J}_{ij}^{(2)}\left(-x_2', y_2; [x, y, z]^{\mathrm{T}}\right), \tag{S62}$$

and now taking advantage of the linearity of integration gives:

$$\mathcal{J}_{ij} = \iint \mathrm{d}x'\mathrm{d}y' \left[\mathcal{J}_{ij}^{(1)}\left(x', y'; [x, y, z]^{\mathrm{T}}\right) + \mathcal{J}_{ij}^{(2)}\left(-x', y'; [x, y, z]^{\mathrm{T}}\right)\right]. \tag{S63}$$

The uglier terms in the above integrand cancel one another, leaving:

$$\mathcal{J}_{ij} = 4\mathcal{A}^2 \iint \mathrm{d}A' \mathrm{Circ}\left(\frac{nr'}{\mathrm{NA}}\right) \frac{\left[\partial_i \theta\left(x', y'; [x, y, z]^{\mathrm{T}}\right)\right]\left[\partial_j \theta\left(x', y'; [x, y, z]^{\mathrm{T}}\right)\right]}{\sqrt{1-(r')^2}}. \tag{S64}$$

Let's now substitute the required derivatives in order to compute each component of $\mathcal{J}$. First the cross terms:

$$\mathcal{J}_{xy} = 4\mathcal{A}^2 k^2 \iint \mathrm{d}A' \mathrm{Circ}\left(\frac{nr'}{\mathrm{NA}}\right) \frac{x'y'}{\sqrt{1-(r')^2}} = 0, \tag{S65a}$$

$$\mathcal{J}_{xz} = 4\mathcal{A}^2 k^2 \iint \mathrm{d}A' \mathrm{Circ}\left(\frac{nr'}{\mathrm{NA}}\right) x' = 0, \tag{S65b}$$

$$\mathcal{J}_{yz} = 4\mathcal{A}^2 k^2 \iint \mathrm{d}A' \mathrm{Circ}\left(\frac{nr'}{\mathrm{NA}}\right) y' = 0, \tag{S65c}$$

where the vanishing of each integral in Eq. (S65) is obtained by noting the parity of the integrands. Next evaluate the diagonal terms:

$$\mathcal{J}_{xx} = 4\mathcal{A}^2 k^2 \iint \mathrm{d}A' \mathrm{Circ}\left(\frac{nr'}{\mathrm{NA}}\right) \frac{(x')^2}{\sqrt{1-(r')^2}} = 4/C_{xy}^2, \tag{S66a}$$

$$\mathcal{J}_{yy} = 4\mathcal{A}^2 k^2 \iint \mathrm{d}A' \mathrm{Circ}\left(\frac{nr'}{\mathrm{NA}}\right) \frac{(y')^2}{\sqrt{1-(r')^2}} = 4/C_{xy}^2, \tag{S66b}$$

$$\mathcal{J}_{xx} = 4\mathcal{A}^2 k^2 \iint \mathrm{d}A' \mathrm{Circ}\left(\frac{nr'}{\mathrm{NA}}\right) \sqrt{1-(r')^2} = 4/C_z^2, \tag{S66c}$$

where $C_{xy}$ and $C_z$ are defined as they are in the main text. Comparing to Eq. (S50), we conclude that $\mathcal{J} = \mathcal{K}$ in this case and thus that this measurement scheme is optimal.

## VII. DETAILS OF NUMERICAL CALCULATIONS

Cramér-Rao bounds were computed numerically using custom MATLAB software. In all cases we assume quasimonochromatic emission of vacuum wavelength $\lambda_\circ = 670$ nm, NA $= 1.4$, and a matched sample-immersion index of $n = 1.518$. Propagation through lenses was simulated via properly scaled implementations of the MATLAB function fft2. Image-plane detection schemes were computed such that calculated images were finely sampled with

20-nm × 20-nm pixels as projected to object space. An exception is the Saddle-Point PSF scheme depicted in Fig. S1; this was more coarsely sampled with 110-nm × 110-nm pixels in order to speed up the optimization. The radial shear interferometer detection scheme was sampled such that the Fourier-plane pixels were approximately of dimensions 0.0027 × 0.0027 in units of NA/$n$. To facilitate fft calculation the Fourier-plane patterns in this case were zero-padded to a total image size of 2048 × 2048 pixels.

## VIII. REFERENCES


[1] Y. Shechtman, S. J. Sahl, A. S. Backer, and W. E. Moerner, Physical Review Letters **113**, 133902 (2014).

[2] Y. Shechtman, L. E. Weiss, A. S. Backer, S. J. Sahl, and W. E. Moerner, Nano Letters **15**, 4194 (2015).

[3] B. Huang, W. Wang, M. Bates, and X. Zhuang, Science **319**, 810 (2008).

[4] S. Jia, J. C. Vaughan, and X. Zhuang, Nature Photonics **8**, 302 (2014).

[5] P. Prabhat, S. Ram, E. S. Ward, and R. J. Ober, IEEE Transactions on Nanobioscience **3**, 237 (2004).

[6] M. Tsang, Optica **2**, 646 (2015).

[7] A. S. Backer and W. E. Moerner, The Journal of Physical Chemistry B **118**, 8313 (2014).

[8] A. Fujiwara and H. Nagaoka, Physics Letters A **201**, 119 (1995).

[9] M. Tsang, R. Nair, and X.-M. Lu, Physical Review X **6**, 031033 (2016).

[10] S. Ragy, M. Jarzyna, and R. Demkowicz-Dobrzański, Physical Review A **94**, 052108 (2016).

[11] L. Pezze, M. A. Ciampini, N. Spagnolo, P. C. Humphreys, A. Datta, I. A. Walmsley, M. Barbieri, F. Sciarrino, and A. Smerzi, Physical Review Letters **119**, 130504 (2017).

[12] A. Fujiwara, Journal of Physics A: Mathematical and General **39**, 12489 (2006).

[13] S. L. Braunstein and C. M. Caves, Physical Review Letters **72**, 3439 (1994).

[14] O. E. Barndorff-Nielsen and R. D. Gill, Journal of Physics A: Mathematical and General **33**, 4481 (2000).

[15] J. W. Goodman, *Introduction to Fourier Optics* (Roberts and Company Publishers, 2005).